Science of the Total Environment 804 (2022) 150165

Contents lists available at ScienceDirect

Science of the Total Environment

journal homepage: www.elsevier.com/locate/scitotenv

Erosion directionality and seasonality study using the *anisotropy matrix*. Application in a semiarid Mediterranean climate (SE Spain)

J. Martínez-Martínez [a,*], A. Abellán [b], E. Berrezueta [c]

[a] Spanish Geological Survey (IGME), Ríos Rosas, 23, 28003 Madrid, Spain
[b] Centre de recherche sur l'environnement alpin (CREALP), Rue de l'Industrie, 45, CH-1950 Sion, Switzerland
[c] Spanish Geological Survey (IGME), Matemático Pedrayes, 25, 33005 Oviedo, Spain

HIGHLIGHTS

- Erosion anisotropy is key for preventive conservation of cultural heritage.
- Wind, wind-driven rain and solar radiation are directional weathering agents.
- A new methodology quantifies the anisotropy degree of the rock weathering system.
- 'Erosion seasonality' is also quantified.
- Results show the most exposed orientations to weathering and erosion.

GRAPHICAL ABSTRACT

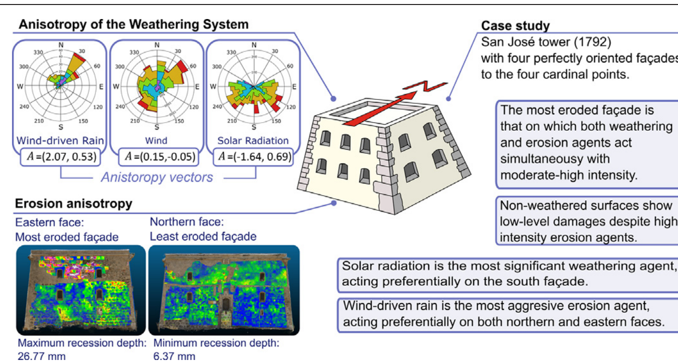

ARTICLE INFO

Article history:
Received 24 May 2021
Received in revised form 1 September 2021
Accepted 2 September 2021
Available online 7 September 2021

Editor: Fernando A.L. Pacheco

Keywords:
Coastal weathering
Aspect
Anisotropy
Calcarenite
Limestone
Building materials

ABSTRACT

This paper is based on the fact that some climatic variables show a preferential directionality and grant a markedly anisotropic character to the weathering system acting on rocks. The aim of this work is to quantify the anisotropic degree of the weathering system and its effects on rock erosion. For this purpose, a new methodology based on the vector analysis of directional and time-dependent parameters is proposed to quantify the annual or seasonal anisotropy of the weathering system. Results show that, on the one hand, wind-driven rain and solar radiation are the most anisotropic variables, being north and east the most intense directions for wind-driven rain and southeast for solar radiation, in the case of the San José Tower, the reference monument of this study. On the other hand, the ranking from the most to the least eroded façades of the tower are: east (maximum recession depth of 26.77 mm) > south (15.53 mm) ≈ west (13.56 mm) > north (6.37 mm). Solar radiation and indirect processes arising therefrom are the most important weathering agents in the semiarid Mediterranean climate, whilst wind-driven rain is the main erosion factor especially due to its torrential character. According to our results, weathering and erosion agents are strongly anisotropic, which emphasizes the importance of integrating the anisotropic character of the weathering system in preventive strategies against surface deterioration of monuments. In this sense, this paper advances the United Nations' 2030 Agenda for Sustainable Development.

1. Introduction

Climate change poses serious threats to the protection and preservation of cultural heritage and, thus, exerts far-reaching socio-economic effects (Fatoric and Seekamp, 2017). Climate change-induced impacts

* Corresponding author.
E-mail addresses: Javier.martinez@igme.es (J. Martínez-Martínez), Antonio.abellan@crealp.vs.ch (A. Abellán), E.berrezueta@igme.es (E. Berrezueta).

https://doi.org/10.1016/j.scitotenv.2021.150165
0048-9697/

on cultural heritage typically include floods, changes in air temperature and humidity values, and extreme weather events, such as storms and droughts (Brimblecombe et al., 2011). Some of these climatic events have a direct impact on cultural heritage (i.e. floods, hurricanes, storms); however, other meteorological parameters have an indirect control over the intensity and frequency of rock weathering processes. For example, temperature and relative humidity cycles condition the aggressiveness of salt weathering in the porous system of rocks (Grossi et al., 2011); or the precipitation regime and minimum temperature ranges determine the effectivity of decay caused by freeze-thaw cycles (Ruedrich et al., 2011). The changing magnitude of these climatic variables has altered the aggressiveness of the weathering system acting on buildings and monuments. This has emphasised the need to identify, quantify and control climatic effects for the development of remedial strategies.

Surface erosion is the last manifestation of rock weathering. Surface erosion is understood as the process in which small components are removed from the rock block by erosion agents (i.e., wind, rain, etc.). Erosion can cause irreparable damage when it occurs on exquisite decorated objects of significant value. However, erosion damage can be considered as moderate or even low when it occurs on low-value elements (i.e. non-visible and/or non-decorated elements). Erkal et al. (2012) introduced two different terms related to material erosion: "surface erosion" and "loss". "Surface erosion" refers to the rock volume lost during the erosion process. In contrast, "loss" incorporates a subjective component related to the appreciation of the eroded piece. This subjective value can be defined in cultural, social, or historical terms. Erkal et al. (2012) quantify the "loss" by a probabilistic approach defined as a function of value, hazard, vulnerability and exposure (Eq. (1)):

$$P_{\text{surface erosion}}(\text{Loss}) = P(\text{Value}) \cdot P(\text{Hazard}) \cdot P(\text{Vulnerability}) \cdot P(\text{Exposure}) \quad (1)$$

The parameter "value" represents the appreciation of the considered element due to its authenticity and the added value of human interaction with the material (Erkal et al., 2012). This subjective parameter ultimately determines when protection or intervention is necessary.

The other parameters (hazard, vulnerability and exposure) can be physically assessed and quantified. "Hazard" refers to the aggressiveness of the weathering system. "Vulnerability" is the lack of resistance to surface erosion of the material. Finally, "exposure" accounts for the façade orientation with respect to the main action directions of weathering agents. "Exposure" also quantifies the time span of weathering actions.

The directionality of weathering processes is a very important issue that has received limited and uneven attention in the literature. Mottershead et al. (2003) point out that the role of aspect – in the sense of direction or position - is important, although the variations brought about by aspect are little understood in practice. The influence of aspect on the weathering processes acting on the rock is broadly accepted but, it has rarely been discussed in detail and remains understudied. According to the bibliographic review included in Mottershead et al. (2003), less than a dozen papers have been published regarding this topic . Most of these are focused on the influence of aspect on the variation of a specific decay agent (Gizzi et al., 2016; McAllister et al., 2017); or describe comprehensive studies of particular cases (Sancho et al., 2003; Demoulin et al., 2016; Martínez-Martínez et al., 2017a; Waragai and Hiki, 2019). All these papers contribute significantly to the background of the question of the anisotropy of the weathering system. However, a far higher number of case studies, different approaches and methodologies are needed to gain a profound knowledge of this topic. The consequences of this deficient general knowledge are aggravated considering the progressive climate change. Climate change is causing variations in the aggressiveness of the weathering system (Grossi et al., 2011; Fatoric and Seekamp, 2017), and most of these variations act in a directional way on buildings, reinforcing and/or modifying the anisotropic character of the exposure environment.

The quantification of the anisotropy of material properties and/or dynamic processes has been broadly treated in bibliography. Several methodologies have been proposed to quantify numerically or graphically the directionality of properties or systems. One of the most comprehensive methodologies for anisotropy quantification uses the matrix analysis (Frydman et al., 2016). In other cases, graphical solutions are found by means of stereographic projections (Almqvist and Mainprice, 2017; Clarke and Vannucchi, 2020) or circular diagrams (Almqvist and Mainprice, 2017; Novitsky et al., 2018). However, the most easy-to-use and direct way to quantify anisotropy is by means of the scalar parameter named "anisotropy ratio" or "percentage of anisotropy" (in %) (Almqvist and Mainprice, 2017; Novitsky et al., 2018; Wu et al., 2020). None of these methodologies, however, have been fully developed for the study of the weathering system, which presents a double problem: spatial anisotropy and temporal variability.

The objectives of this research are, on the one hand, to propose a new methodology for the analysis and quantification of the directionality of the weathering system. This methodology is focused on the achievement of a general view of the anisotropic character of the exposure environment, offering a step forward the comprehensive understanding of this problem. New parameters are proposed in order to obtain a total anisotropic factor specifically calculated for each site. On the other hand, this new methodology is applied to the analysis of the weathering system and the erosion of calcarenites and limestones used as building rocks in the San José Tower of Nueva Tabarca Island (SE Spain). This monument provides a relevant case study under semi-arid Mediterranean climate. The studied rock weathering system is analysed in terms of "hazard", "vulnerability" and "exposure", and its anisotropic character is quantified using the proposed methodology.

2. The anisotropic and isotropic components of weathering systems

The proposed method divides the global weathering system into two subsystems: 1) an isotropic background that defines global conditions acting over all the surfaces with similar magnitudes; and 2) an anisotropic component that includes all the directional climatic variables that modify the global conditions and/or add new weathering processes to specific exposures.

The isotropic component is defined by air temperature, relative humidity, and the precipitation regime. All these parameters are scalar time-dependent variables. Consequently, their magnitude and their temporal variation can be quantified by means of descriptive statistics, such as mode, median, mean and/or different percentiles. Some authors propose equations to obtain meteorological parameters that quantify the environmental aggressiveness (i.e., daily thermal range, number of hygric transitions crossing certain threshold, etc.) (see examples in Brimblecombe et al., 2011).

The anisotropic subsystem is formed by directional variables: wind, wind-driven rain, and solar radiation. Each one of these is a vector time-dependent variable, so they are defined in a given moment t by a magnitude, an orientation and a specific sense.

3. Study site

3.1. San José Tower and Nueva Tabarca Island

San José Tower was built in 1792, and it constitutes the last built element of a defensive complex designed and partially erected throughout the 18th century in Nueva Tabarca Island (SE of Spain) (Fig. 1) (Martínez-Martínez et al., 2017a). San José Tower is located in the geographic centre of the island, and it is one of the most emblematic elements of the local heritage. The 27-m-high tower is a four-sided structure with a slightly rectangular planform. i action has wide and flat façades oriented almost perfectly to the four cardinal points

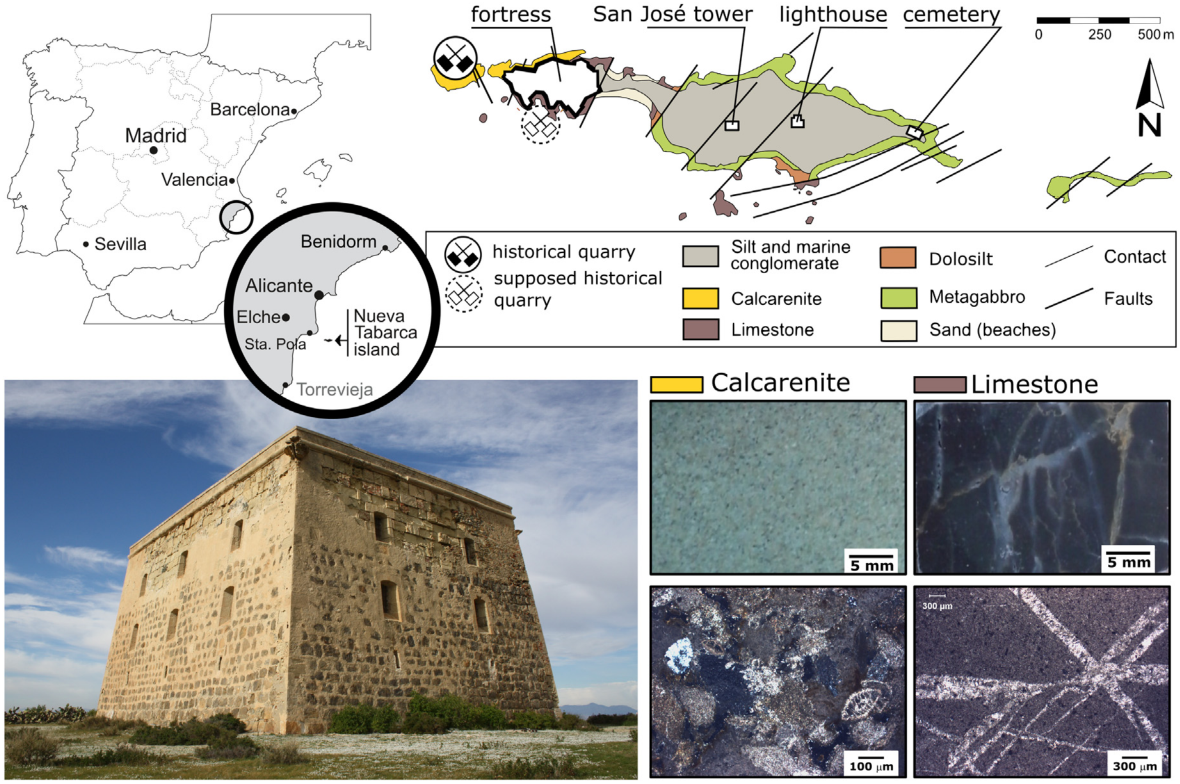

Fig. 1. Upper left: Situation map and location of Nueva Tabarca Island. Down left: image of the San José Tower. Down right: macroscopic (hand sample) and microscopic views of the building materials.

(deviation of 7°). All the façades are slightly leaning from the vertical position (around 5°) (Fig. 1). This configuration creates differentiated weathering micro-environments representative of the four cardinal points.

Tower location is in a completely flat plain and, due to the absence of sheltering structures, all the faces receive seaward exposure.

3.2. Building materials

From a constructive point of view, two different levels can be recognized in the monument (Fig. 2). The lower two thirds of the building were mostly built using medium-sized rough-ashlars of a massive grey limestone (Fig. 1). The building corners were reinforced using big ashlars of a local yellowish calcarenite. The upper part was constructed using exclusively regular blocks of calcarenite. Due to the advanced state of deterioration, some parts of the building were rebuilt during the last decades of the 20th century using bricks, pebbles from local beaches and reused materials (Fig. 2).

Both building rocks, the yellowish calcarenite and the grey limestone, were extracted from local outcrops (Fig. 1) (Corbí et al., 2019). Calcarenite blocks were obtained from the sedimentary Miocene deposit located in *La Cantera* Islet (Martínez-Martínez et al., 2017b).

Fig. 2. Constructive sketches of the four façades of the San José Tower.

Table 1
Porous system characterization and hydro-mechanic properties of the studied rocks. χ: mean values; [min-max]: minimum to maximum values range.

	Calcarenite		Limestone	
	χ	[min-max]	χ	[min-max]
Open porosity [%]	20.66	[16.15–24.13]	0.99	[0.55–1.42]
Mean pore radius [μm]	0.20	[0.10–0.37]	1.94	[1.6–2.41]
Capillary coefficient [$Kg/m^2h^{0.5}$]	6.88	[2.88–11.65]	0.93	[0.44–1.65]
Rock strength [MPa]	32.29	[19.69–44.22]	94.52	[70.48–110.10]
Dry weight loss [%]	20.56	[0.11–78.59]	0.50	[0.2–0.77]

Grey limestones outcrop in the central part of the Nueva Tabarca Island (Fig. 1), but no information or evidence of the exact quarrying area has been preserved.

Table 1 presents the petrophysical and hydro-mechanical properties of both building rocks. The porous system of the rocks was characterized by means of the values of open porosity and mean pore radius. The open porosity was calculated using the vacuum water saturation test (after UNE-EN 14157). Mean pore size was measured by means of mercury porosimetry (MIP). Capillary coefficient is the sorptivity expressed in $kg/m^2h^{0.5}$, and it was obtained according to ASTM D5731. Rock strength was determined by means of the Point Load Test following the methodology proposed in UNE-EN 12370. Rock durability was assessed via a salt crystallization test. Five samples of each kind of lithofacies were tested, and a 14% *w*/w Na_2SO_4 solution was used, in accordance with the UNE-EN-12370 recommendations. The dry weight loss at the end of the 50 cycles of salt crystallization test was used to evaluate the resistance to salt weathering.

The calcarenite and the grey limestone show considerable differences in terms of porosity and hydro-mechanical behaviour. Calcarenites have an open, well-connected porous system that reaches 24% of the rock volume. Contrarily, grey limestones are dense materials with small, poorly connected pores (mainly fissures of ~2 μm width). The characteristics of the porous system control water transport through the rock; consequently, conditions for water movement are more favourable in the calcarenite than in the limestone (see values of capillary coefficient in Table 1). Mechanically, limestones are stronger than calcarenites, and their resistance to salt weathering is also higher.

3.3. Conservation state and weathering patterns

The aggressiveness of the local environment and the low suitability of the used building stones resulted in the fast deterioration of monuments in Nueva Tabarca Island. Despite restoration works on the San José Tower during the last decades, dissimilar erosion states can be observed on each façade. One of the objectives of this work is to quantify the degree of erosion precisely despite the inaccessibility of the studied surfaces (a 27-m high tower). In order to solve this problem, the erosion quantification was carried out by means a methodology based on 3D photogrammetric models (see following subsection).

Calcarenite and limestone blocks used in the architectural heritage of Nueva Tabarca Island show differences both in weathering patterns and intensity degrees (Fig. 3). On the one hand, rounding forms (Fig. 3A), alveolization (Fig. 3B) and differential erosion forms (Fig. 3C) predominate in the calcarenite ashlars (terminology used according to ICOMOS ISCS glossary, ICOMOS-ISCS, 2008) (Fig. 3). Microkarsting and thin dust films are the preferential weathering patterns observed on limestone ashlars (Fig. 3D). Higher intensity degrees are always observed on the calcarenite weathering forms.

4. Methods

4.1. 3D photogrammetric model and surface erosion quantification

In order to quantify the erosion degree on each one of the four façades of the San José Tower, a high-resolution 3D photogrammetric model was obtained. Firstly, a photographic campaign was carried out using a multi-rotor unmanned aerial vehicle (UAV) to obtain high quality images of the façades in accessible and non-accessible areas from different angle views and distances (Stumpf et al., 2013). A set of 548 photographs was taken using a Phantom III Advanced UAV system. This device includes a 12-megapixel camera with a 20 mm (35 mm equivalent) lens and an in-built unit, which collects GPS position and orientation data for each picture. These images were acquired covering a series of surrounding continuous tracks over a one-hour period in sunny conditions. Photographs were collected with 60-70% overlap between adjacent images, with a camera orientation orthogonal to the surface according to Micheletti et al., 2015. Two sets of photographs were acquired with distances ranging between 5 and 15 m. After photograph acquisition, the 3D digital model of the tower was developed by processing images using the SfM photogrammetric software (Agisoft Photoscan ©) following the standard workflow for DEM generation without ground control points (Agisoft, 2017). Key-point detection and matching aligned the 548 photographs into a single 3D sparse point cloud. Subsequent dense point cloud was computed at medium quality, resulting in a 3D model with an average point spacing of 0.005 m. The tower model was converted into a real-world reference

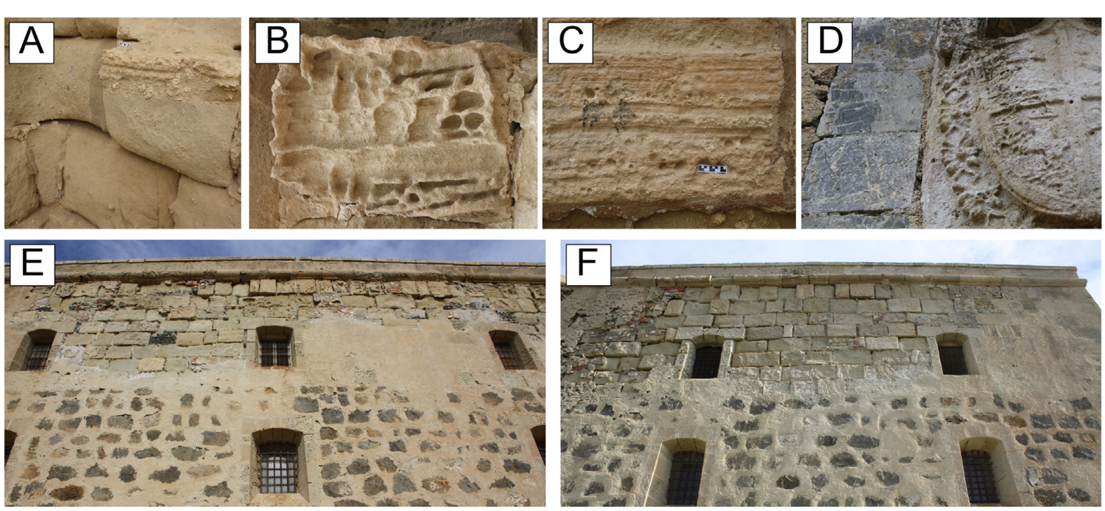

Fig. 3. Weathering patterns observed on the architectural heritage of Nueva Tabarca Island. A-D: examples of weathering forms (A, rounded ashlars; B, alveolization; C, differential erosion; D, microkarsting in grey limestone and slight alveolization in calcarenite). E-F: general view of the most eroded areas of the San José Tower (E, south façade; F, west façade).

frame using the positions of the images recorded by the in-built GPS device of the aircraft.

The 3D photogrammetric model was the base to quantify the erosion intensity at each one of the four main façades of the San José Tower. A hypothetical non-eroded covering surface was defined overlapping the eroded modelled surfaces. These theoretical original surfaces were defined taking into account those areas in the façades where unweathered original plaster has been preserved (Fig. 2). A flat surface joins all these non-eroded areas and constitutes the reference layer (erosion intensity equals zero). Numerical comparison between the two surfaces was carried out by means of the 3D point cloud processing software Cloudcompare ©. Erosion intensity was quantified by means of the *Recession* parameter (measured in mm). This parameter is defined as the difference between the two point clouds using well-established 3D point cloud comparison procedures (Laque et al., 2013). Results were obtained every 10 cm throughout the entire tower surface, and more than 350,000 measurements were made per façade. Data were processed for each façade individually, differentiating in each case the upper part (calcarenite section, Fig. 2) and the lower part (limestone section, Fig. 2).

4.2. Climatic and micro-environmental data acquisition

Nueva Tabarca Island climatic parameters were measured with the aid of a weather station (Davis-Wireless Vantage PRO2) which included a tipping-bucket rain gauge (Davis 7852) for rainfall measurements, an anemometer and a 12-bit smart Sensor (Davis 7315) to measure the relative humidity and air temperature with an accuracy of ±0.5 °C above -7 °C, and ± 2% from 10% to 100% RH. These parameters were recorded every 30 min from April 2009 to February 2011. The Data Acquisition System consisted of a WeatherLink (#6510) data logger. Unfortunately, due to the corrosive environment of the island, electronic problems caused gaps in the data log during the measurement period.

Wind-driven rain was obtained from combining rainfall and wind data according to Blocken and Carmeliet (2010). Wind-driven rain load (R_{wdr}) on buildings is calculated according to:

$$R_{wdr} = \alpha \cdot U \cdot R_h^{0.88} \cdot cos\beta \tag{2}$$

Where α is the adapted WDR coefficient (s/m), which takes into consideration the site topography and the presence of buildings. U (m/s) is the reference wind speed measured at the standard meteorological height of 10 m. R_h is the unobstructed rainfall intensity and β is the wind incidence angle between wind direction and the normal vector of the wall surface. In this study, WDR coefficient takes values from 0.04 s/m (when z < 2 m) to 0.13 s/m at the top of the tower.

Data of global solar radiation on the Nueva Tabarca Island was obtained from the database of the Spanish State Meteorology Agency (AEMET), assuming that the values at the study point are comparable to those measured at the nearest weather station of the national observation network (El Altet station; 13 km away).

Directional climatic parameters (wind, wind-driven rain, and solar radiation) were projected on the 3D photogrammetric model of the tower. For this purpose, the 3D model was georeferenced, and the normal vector of each oriented façade was calculated. The partial intensity of both wind and wind-driven rain acting on the four surfaces of the tower were calculated decomposing them into each normal vector following the "cosine projection method" (Blocken and Carmeliet, 2006). Direct insolation on each one of the walls was calculated taking into account both the sun position through the day and year and the specific normal vector of each façade (following the algorithm and workflow of Fu and Rich, 1999).

4.2.1. Microclimatic characterization

Specific microclimatic conditions on the north and south façades were recorded during two 48-h campaigns (23th-24th January and 4th-5th August). Two T-RH sensors (HOBO U23 Pro v2 data logger) were positioned a few centimetres from the south and north walls to record the local micro-environment. Sensors were protected from the direct sun radiation by a white screen. Air temperature and relative humidity values were saved every 30 min. Air temperature was measured with an accuracy of ±0.2 °C over 0° to 50 °C. The relative humidity sensor operated over a RH range from 0 to 100% with a minimum accuracy of ±3.5% (above 95%). In addition, a manual thermometer and hygrometer (Vaisala HMP75) was used to calibrate the continuous recording and to measure specific climatic conditions around the monument.

Global distribution of surface temperature on all four façades and their daily thermal evolution was determined using a thermal imaging camera. Two sequences of 5 thermal imaging sets were carried out at different hours (21:00, 00:30, 02:30, 10:30, 15:00) during the micro-environmental analysis campaigns.

4.3. Calculation of weathering system anisotropy

Directional variables (wind, wind-driven rain, and solar radiation) are vector time-dependent variables, so they are defined in a given moment t by a magnitude, an orientation and a specific sense. In order to operate with this vector system, each directional variable ($\overrightarrow{v}$) is decomposed into three components along the north-south (v_{NS}), east-west (v_{EW}) and vertical (zenith) (v_Z) axes applying the cosine projection method (Blocken and Carmeliet, 2010) (Eq. (3)). For vertical walls and structures, the zenith component is not considered. v_{NS} and v_{EW} can be subdivided into two components each, transforming the initial vector into a four-dimensional vector (Eq. (4)).

$$\overrightarrow{v} = (v_{NS}, v_{EW}, v_Z) \tag{3}$$

$$\overrightarrow{v} = (v_N, v_S, v_E, v_W);\ where \left\{ \begin{array}{c} v_N = v_{NS}\ when\ v_{NS} > 0;\ and\ v_N = 0\ when\ v_{NS} < 0 \\ v_S = |v_{NS}|\ when\ v_{NS} < 0;\ and\ v_S = 0\ when\ v_{NS} > 0 \\ v_E = v_{EW}\ when\ v_{EW} > 0;\ and\ v_E = 0\ when\ v_{EW} < 0 \\ v_W = |v_{EW}|\ when\ v_{EW} < 0;\ and\ v_W = 0\ when\ v_{EW} > 0 \end{array} \right\} \tag{4}$$

A discrete event (i.e., a windy event during a time span close to 0) is defined by the value of its NS and EW components (v_{NS} and v_{WE}; or v_N, v_S, v_E, v_W). A continuous event (monitored during a specific time span (t) can be quantified by the mean value of its NS and EW components ($\overline{v}_N^t$, $\overline{v}_S^t$, $\overline{v}_E^t$ and $\overline{v}_W^t$, in Eq. (5)) or by the accumulated effect on each of the four main cardinal directions (v_N, v_S, v_E and v_W in Eq. (6)). n in Eq. (5) is the number of samples in which the monitored variable is different to 0.

$$\overrightarrow{v}^t = (\overline{v}_N^t, \overline{v}_S^t, \overline{v}_E^t, \overline{v}_W^t) = \left(\frac{\sum_{i=1}^{i=t} v_N^i}{n}, \frac{\sum_{i=1}^{i=t} v_S^i}{n}, \frac{\sum_{i=1}^{i=t} v_E^i}{n}, \frac{\sum_{i=1}^{i=t} v_W^i}{n} \right) \tag{5}$$

$$\overline{v}_{acc}^t = (\overline{v}_{acc}^t, \overline{v}_{acc}^t, \overline{v}_{acc}^t, \overline{v}_{acc}^t) = \left(\sum_{i=1}^{i=t} v_N^i,\ \sum_{i=1}^{i=t} v_S^i,\ \sum_{i=1}^{i=t} v_E^i,\ \sum_{i=1}^{i=t} v_W^i \right) \tag{6}$$

The anisotropy vector ($\overrightarrow{A_v}$) and the normalized anisotropy vector ($\overrightarrow{A_v^n}$) associated to a directional variable, monitored during a continuous period of time (t) are defined according to Eqs. (7) and (8), respectively.

$$\overrightarrow{A_v} = \left(\sum_{i=1}^{i=t} \left(v_N^i - v_S^i \right), \sum_{i=1}^{i=t} \left(v_E^i - v_W^i \right) \right) \tag{7}$$

$$\left(\overrightarrow{A_v^n} \right) = \left(\frac{\sum_{i=1}^{i=t} (v_N^i - v_S^i)}{\sum_{i=1}^{i=t} (v_N^i + v_E^i + v_S^i + v_W^i)/4}, \frac{\sum_{i=1}^{i=t} (v_E^i - v_W^i)}{\sum_{i=1}^{i=t} (v_N^i + v_E^i + v_S^i + v_W^i)/4} \right) \tag{8}$$

The anisotropy of a discrete directional event ($t_0 = t_f$) is maximum. However, the anisotropic character of a continuous directional event ($t_0 \neq t_f$) depends on the real prevalence of a few preferential acting directions over the rest. The closest each component is to 0, the most isotropic is the considered variable in that direction. Positive values in the first or the second component mean a northern or eastern predominance, respectively. In turn, negative values represent southern predominance (in the first component) and western predominance (in the second one). The modulus of the anisotropy vector quantifies the anisotropic character of the considered directional variable. The higher the modulus, the more anisotropic the weathering system.

Considering the anisotropic vector of the three main directional variables of weathering systems acting on rock ($\overrightarrow{A_w}$ for wind, $\overrightarrow{A_{wdr}}$ for wind-driven rain and $\overrightarrow{A_{sr}}$ for solar radiation), the anisotropy matrix can be defined (Eq. (9)).

$$[A] = \begin{bmatrix} \left(\overrightarrow{A_w}\right) \\ \left(\overrightarrow{A_{wdr}}\right) \\ \left(\overrightarrow{A_{sr}}\right) \end{bmatrix} = \begin{bmatrix} (w_N - w_S) & (w_E - w_W) \\ (wdr_N - wdr_S) & (wdr_E - wdr_W) \\ (sr_N - sr_S) & (sr_E - sr_W) \end{bmatrix} \tag{9}$$

The anisotropy matrix [A] is time dependent; consequently, [A] can be calculated for a daily, monthly, seasonal or yearly periodicity. Results provide information about the variability of the anisotropic character of the exposure environment, and it is possible to define a constant anisotropic character along the year, or contrarily, a seasonal anisotropy.

5. Results

5.1. Surface erosion

In general terms, the four studied façades show similar erosion profiles (Fig. 4), in which two parts can be recognized: the lower areas of the façades (built with grey limestone ashlars, Fig. 2) where minimum or zero recession depths are measured; and the upper areas (calcarenite zone, Fig. 2) with medium-maximum recession depths (Fig. 4). Erosive forms in the upper area vary from one ashlar to another. Rounding forms prevail in general terms, but alveolization and differential erosion patterns can also be observed. The numerical analysis of the recession depths was carried out separately in the upper and lower zone of each façade (calcarenite and limestone zone, respectively). Fig. 5 includes both the partial histograms and the accumulative curves of the surface recession measurements obtained on the four studied façades (north, east, south and west façades). Included tables show the quantification of each distribution by means of their percentiles (25th, 50th, 75th, 95th and 99th percentile).

Curves and data showed in Fig. 5 completes the above general overview of the façades with quantitative information. The four partial histograms of the lower zone (limestones) present similar patterns, and the associated percentiles are quite close to each other. The maximum difference between the mean recession depth (50th percentile) was registered between the north and south faces and has a value of 0.66 mm. The difference is 1.93 mm considering the 99th percentile.

Contrarily, surface recession histograms in the upper part (calcarenite zone) vary strongly from one face to another. Maximum differences are registered between east and north façades with values of 4.95 mm and 20.4 mm (50th and 99th percentiles, respectively). The ranking from the most to the least eroded façades is east>south≈west>north.

Despite the step forward in the erosion quantification of inaccessible surfaces by means of the 3D photogrammetric models (i.e., the 27-meter high San José Tower), future research lines will be developed to obtain higher resolution in the reconstructed images. These future works will allow researchers to recognize the different weathering patterns developed in each ashlar and to quantify recession profiles on each individual block.

5.2. Climatic conditions

5.2.1. Non-directional climatic parameters: air temperature, relative humidity, and rainfall

Local climatic data of Nueva Tabarca Island during the period April 2009 to February 2011, expressed as monthly averages, are shown in Table 2. Air temperature and relative humidity are expressed in percentiles (5th, 25 th, 50 th, 75 th and 95 th) per month. Rainfall is quantified through the parameters accumulated rainfall per month and monthly duration of precipitations. Yearly mean values (×) of each parameter are also included in Table 2.

A Mediterranean semiarid climate ("Csa" according to the Köppen-Geiger climate classification) dominates the geographic area of the island, with an annual average temperature of 19.3 °C and a strong seasonality. The lowest temperatures are recorded from December to February and can reach minimum values of 3.6 °C. The maximum temperature during the registered period was 31.6 °C (August). Daily thermal oscillation is moderate-low, registering an almost constant average

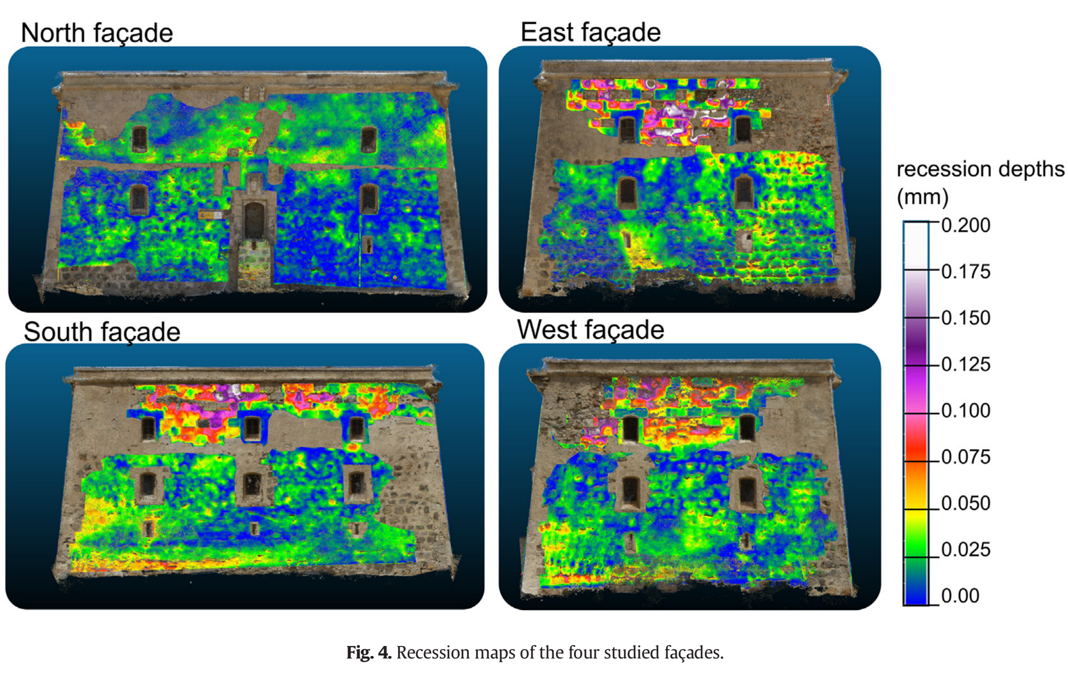

Fig. 4. Recession maps of the four studied façades.

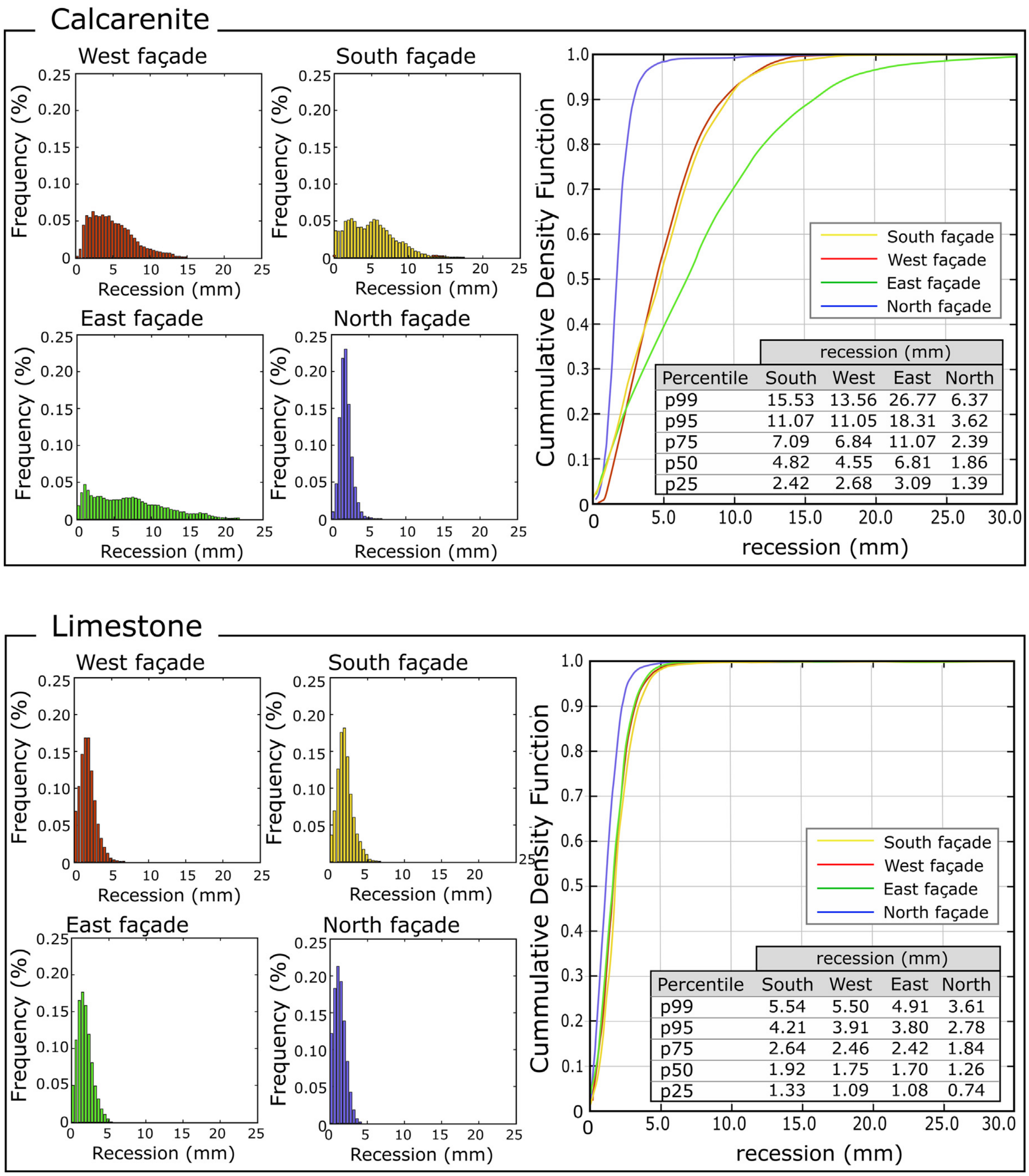

Fig. 5. Partial histograms and cumulative functions of the recession measured on the four façades. Tables show the recession depths measured on each façade (expressed in percentiles).

value of 4.3 °C throughout the year. However, wide thermal ranges can be measured occasionally. For example, a maximum daily thermal range of 9.4 °C was registered in December.

The relative humidity is high due to the proximity of the sea, with an average annual value of 74.3%. The seasonal fluctuation is low; the minimum relative humidity registered during the driest months (autumn-winter) ranged between 32.2 and 36.5% and the minimum value during the wettest period (summer) was 50.3%. Maximum values close to 90% are detected in each month. Daily fluctuations, however, can be significant, with a variation from 80% to 40% during a 12-hour period.

The region is characterized by relatively low annual rainfall (251 mm during the registered period), in accordance with the prevailing semiarid climate. During summer, there are long periods of drought, with only short and occasional rainfalls. The maximum rainfall is in autumn and, especially, winter. Torrential rains are characteristic in this period. For instance, extreme 24 h long rainfalls were recorded on 2 March 2010 (66.6 mm) and 27 January 2011 (44.3 mm). Most of this rainfall volume occurred in a two-hour period.

5.2.2. Directional climatic parameters: wind, wind-driven rain, and solar radiation

Table 3 includes the intensity of different directional climatic parameters. Wind speed is expressed in percentiles (5th, 25 th, 50 th, 75 th and 95 th) per month. Total wind-driven rain is quantified by the accumulated action and intensity of the maximum event per month. Global radiation is expressed in the maximum radiation registered per month and the monthly mean. Yearly mean values (×) of each parameter are also included in Table 3.

Fig. 6 shows the spatial distribution of each variable. The intensity of a variable in a specific orientation is expressed with different percentiles

Table 2
Non-directional climatic data (air temperature, relative humidity, and rainfall) of Nueva Tabarca Island. χ: annual values.

	Air Temperature [°C]					Relative Humidity [%]					Total rainfall [mm]	
	P5	P25	P50	P75	P95	P5	P25	P50	P75	P95	Cum.	Hours
χ	15.7	17.6	18.9	20.1	22.0	54	70	78	85	90	21.1	10.5
Jan	9.1	10.9	12.3	13.8	16.0	54	72	80	87	92	45.8	5.0
Feb	8.3	10.4	12.9	14.4	16.6	45	66	79	86	92	67.5	42.0
Mar	8.9	11.6	13.2	14.4	16.8	50	73	81	90	94	74.6	16.0
Apr	14.7	16.0	16.9	17.8	19.6	52	66	76	83	90	0.0	0.0
May	16.2	18.2	19.3	20.6	22.1	67	77	83	88	92	3.2	5.5
Jun	20.1	22.1	23.2	24.4	25.8	61	77	81	86	90	0.0	0.0
Jul	24.1	25.1	26.1	26.9	28.3	67	78	83	87	91	0.2	0.5
Aug	25.1	25.9	26.6	27.7	28.8	66	75	79	83	87	42.1	3.0
Sep	22.9	24.2	24.9	25.7	27.7	51	67	72	77	84	0.0	0.0
Oct	18.6	19.8	21.1	22.0	23.6	51	70	76	84	90	4.6	5.0
Nov	13.2	16.3	18.1	19.6	21.9	43	56	75	84	89	3.6	3.0
Dec	6.8	10.6	12.5	14.4	16.6	48	64	79	87	92	11.0	14.5

in order to identify the directions of the most aggressive events (events above 95th percentile).

Nueva Tabarca Island has a seasonal wind regime. On the one hand, eastern winds prevail during summer (from May to September), with directions ranging between N50E to N110E. On the other hand, SW and WNW directions are preferentially registered from the end of autumn (November) to February. These preferential directions vary slightly when only winds of the highest energy are considered (events above the 95th percentile in Fig. 6). In this case, summer winds (from July to September) tend to blow with NE directions (between N40E and N65E), whilst autumn winds (from September to November) have SWS directions (ranging from N195E to N220E).

Total wind-driven rain in Nueva Tabarca Island is 408.13 mm ¿per year?. Interpreting this result according to the reference values proposed in the Lacy classification (Lacy and Shellard, 1962), San José Tower has a "moderate exposure" in general terms. However, during most part of the year, the exposure is "sheltered", for wind-driven rain is only significant a few months per year (in summer and winter). The most intense wind-driven events occur with NEN direction (Fig. 6).

Solar radiation shows high values during the whole year, due to both the relative low latitude of the case study and the extremely few cloudy days registered along the year. The maximum values measured in early summer (June-July, Table 3) reach 360 W/m^2. The minimum value measured at noon was 35 W/m^2 (December).

Table 3
Directional climatic data (wind speed, total wind-driven rain, and global radiation) of Nueva Tabarca Island. χ: annual values.

	Wind speed [m/s]					Total wind-driven rain [mm/h]		Global radiation [W/m^2]	
	P5	P25	P50	P75	P95	Cum.	Max	Max	Monthly mean
χ	1.4	4.6	8.8	14.5	19.6	34.05	9.77		
Jan	1.1	5.1	8.7	14.5	18.2	62.4	28.0	219	60.4
Feb	1.3	5.6	10.3	14.3	17.4	125.7	9.6	261	70.1
Mar	1.4	5.5	9.2	16.7	23.8	113.48	31.1	319	101.6
Apr	3.2	4.2	10.5	17.9	22.2	0.0	0.0	344	158.9
May	1.6	3.8	8.4	14.1	18.7	3.89	1.2	345	171.6
Jun	1.8	3.5	8.0	15.0	19.5	0.0	0.0	360	189.8
Jul	1.8	5.4	7.2	15.8	24.1	0.6	1.5	360	189.4
Aug	0.0	3.8	7.0	12.4	16.0	80.8	37.5	343	163.1
Sep	1.5	4.1	8.7	11.1	15.5	0.0	0.0	322	118.6
Oct	0.0	3.4	7.8	14.3	19.6	10.2	6.6	246	90.9
Nov	1.4	5.8	10.9	15.5	20.1	3.6	1.1	216	72.0
Dec	1.6	5.3	8.7	16.3	20.4	7.9	0.6	191	53.2

5.3. Anisotropy of the weathering system

Fig. 7 shows the annual evolution (cumulative function) of the north, east, south and west components of each directional variable. The partial accumulated values (Δ) per façade at the end of each season are included in the corresponding graph. The final accumulated values and the average intensity per event are also expressed in Fig. 7. The annual anisotropy matrix ($[A]_{year}$, Eq. (10)) and the seasonal anisotropy matrix (Eq. (11)–(14)) were obtained according to Eq. (9).

$$[A]_{year} = \begin{bmatrix} 0.15 & -0.05 \\ 2.07 & 0.53 \\ -1.64 & 0.69 \end{bmatrix} \tag{10}$$

$$[A]_{spring} = \begin{bmatrix} 0.76 & -0.17 \\ 2.10 & 0.28 \\ -2.36 & 0.84 \end{bmatrix} \tag{11}$$

$$[A]_{summer} = \begin{bmatrix} -0.59 & 0.11 \\ 2.08 & -0.14 \\ -1.07 & 0.70 \end{bmatrix} \tag{12}$$

$$[A]_{autumn} = \begin{bmatrix} 0.29 & 0.46 \\ 2.06 & 1.85 \\ -1.24 & 0.69 \end{bmatrix} \tag{13}$$

$$[A]_{winter} = \begin{bmatrix} 0.00 & -0.45 \\ 1.50 & 1.27 \\ -2.56 & 0.53 \end{bmatrix} \tag{14}$$

The most anisotropic variables are wind-driven rain and solar radiation (Eq. (10)). Wind also shows a slight directionality in spring (North) and summer (South), but this seasonal anisotropy is compensated on the annual scale and displays a quasi-isotropic behaviour (Eq. (10)).

Wind-driven rain is highly anisotropic ($\overrightarrow{A}^{n}_{wdr}$=(2.07,0.53)). During spring and summer, wind-driven rain has a clear northern directionality (Eqs. (11) and (12), respectively), but winter and autumn episodes, which are the most intensive ones, have a distinct north-east component (Eqs. (13) and (14), respectively). This anisotropic behaviour is clearly shown in Fig. 7. The flat sections in the cumulative wind-

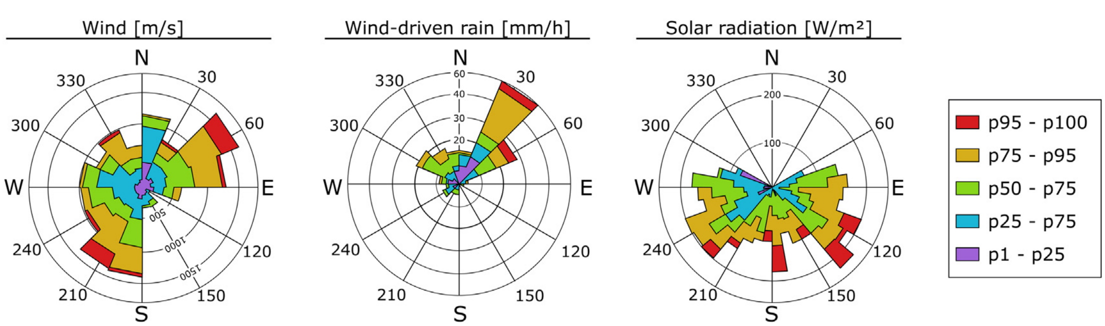

Fig. 6. Rose diagrams of the studied directional climatic parameters. (For interpretation of the references to colour in this figure legend, the reader is referred to the web version of this article.)

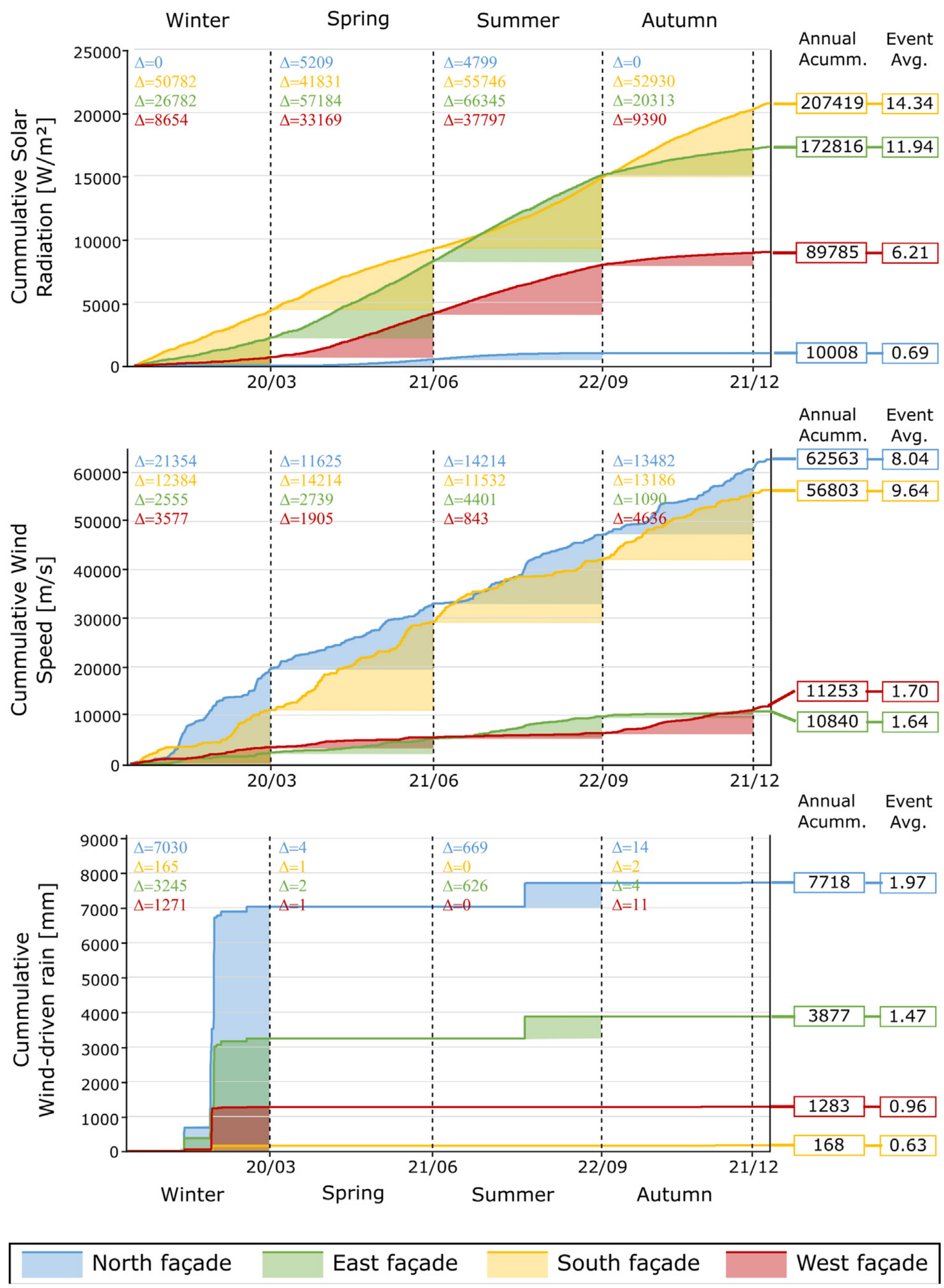

Fig. 7. Annual evolution (cumulative function) of the north, east, south and west components of each directional variable.

driven rain curves correspond to the prolonged droughts that characterize the semiarid Mediterranean climate. These droughts can last more than 3 months, and wind driven rain during these periods is equal to zero (no increments in the cumulative curves). Sporadic torrential rains occur preferentially in autumn and winter, and they are markedly directional according to the results obtained in this work.

Solar radiation ($\overrightarrow{A}^{n}_{sr}$=(-1.64,0.69)) shows a clear directionality with seasonal variation. The north façade only receives weak solar radiation around the summer solstice. Contrarily, the south face is irradiated during the whole year, but maximum values on this surface are registered in spring and winter (see variable evolution in Fig. 7). Summer values of solar radiation are lower on the south façade due to the high sun elevation and the resulting high incidence angle. East and west façades receive a variable radiation with maximum in summer and minimum during wintertime. A moderate positive anisotropy is found in the east-west direction indicating a higher solar radiation on eastern faces.

5.4. Influence of solar radiation on surface temperature

All stone blocks suffer large-scale temperature fluctuations related to both annual and daily cycles of air temperature (non-directional variable) (Díez-Herrero et al., 2009; McAllister et al., 2017). These variations are isotropic and affect all exposures. However, secondary small-scale fluctuations generated by direct solar radiation are superimposed on the previous one. These are strongly anisotropic and affect southern exposures particularly. These small-scale fluctuations can show high intensity and amplitude, but their influence is restricted to the outer few millimetres of the stone (McAllister et al., 2017).

Specific measurements carried out on the north and south façades of the San José Tower revealed both small and large-scale thermal fluctuations (Fig. 8A and B). On the one hand, surface temperatures in August are 20 °C higher than those measured in January, defining significant large-scale thermal variation along the year. On the other hand, hourly measurements demonstrated that rock surface temperature is closely related to air temperature. This is especially noticeable on the north face, where solar radiation influence on surface temperature is practically negligible and, consequently, surface temperature is a function of air temperature (Fig. 8A). The rest of the façades, however, undergo rapid temperature increases when radiated. Southern façades registered increments of surface temperature with respect to northern ones that can reach 17.5 °C during periods of maximum solar exposure (Fig. 8A). Moreover, eastern and western façades also suffer significant surface temperature increase at sunrise and sunset, respectively. After radiation, surface and air temperature trend to coalesce.

Calcarenite shows a more sensitive thermal response to solar radiation than limestone its surface temperature increases up to 3 °C more during the daily cycle (fig. 8B). This can be justified with the higher porosity and better-connected porous system of calcarenites that allows a more efficient heat transfer (see porosity values in Table 1). However, this difference between calcarenite and limestone blocks is less significant during summertime, when the two rocks show almost the same thermal response.

6. Discussion

6.1. Analysis of the variation of rock erosion rates according to the anisotropy matrix of the weathering system

The erosion intensity of the calcarenite blocks of the upper part of the San José Tower has an aspect-related variability. The most eroded ashlars are those located in the east façade, and the least affected ones are those oriented to the north. The fact that the northern surface shows a very low erosion intensity (Figs. 4 and 5) indicates that the aggressiveness of the isotropic component of the weathering system is low and, therefore, the observed erosion must be caused by the directional climatic variables (anisotropic component).

Wind in coastal regions is an important decay agent, especially due to its ability to drive salty water deep into the fabric of building and to move abrasive sand by saltation (Shi and Shi, 2014; Zhao et al., 2016). In fact, wind-blown sand is one of the most destructive agents related to aeolian erosion (Zhao et al., 2016). This process is not uncommon in the area of the San José Tower due to its proximity to sandy pavements from where particles can be mobilized (Martínez-Martínez et al., 2017a). Taking into account the different exposure of each façade to winds (Fig. 6), north and south orientations are expected to be the most affected by aeolian erosion. However, wind-blown sand cannot justify the observed erosion in the calcarenite blocks because they are situated in the upper part of the tower (above 15 m) and the maximum abrasion related to sand impacts occurs close to the ground. Shi and Shi (2014) concluded that the erosion damage caused by wind-blown sand has a stratification pattern in which three layers are recognized with the increment of height. The first of these layers (the one closest to the ground) shows an upward increase of abrasive capacity, the second one is the saturation layer (where the maximum abrasion occurs), and the last one is the decrement layer. In this profile, the maximum abrasion rate is found at a certain height above the ground. Shi and Shi obtained the maximum point at 22 mm when wind speed is 0.51 m/s and the diameter of sand particles is 0.3 mm.

Surface thermal changes caused by solar radiation can act as a key control over the operation and effectiveness of stone decay processes (Díez-Herrero et al., 2009). In fact, it is generally accepted that temperature exercises a critical control over the efficacy of weathering processes and the occurrence and severity of the caused stone decay (Hall et al., 2012). Temperature may induce stresses through differential heating and differential thermal expansion between rock components, as well as between the rock and salts present in the porous system (Benavente et al., 2008). In addition, temperature also has an impact on moisture availability and movement through the porous system of rocks, determining evaporation processes and, consequently,

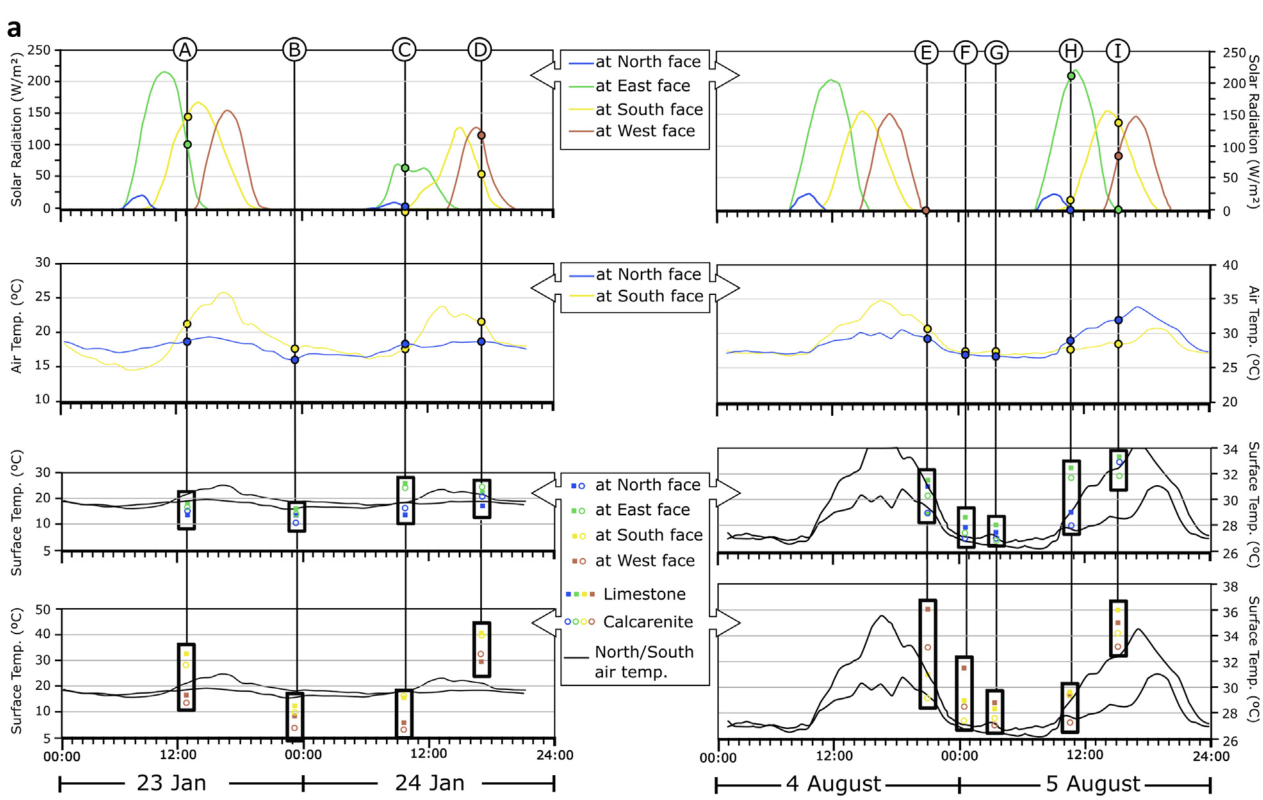

Fig. 8A. Correlation between solar radiation and temperature evolution in winter (23th-24th January) and summer (4th-5th August). Letters A-I refer to the punctual measurements carried out with thermographic camera. Corresponding thermographic images are shown in Fig. 8B.
B. Thermographic images obtained during the winter and summer campaigns. Image letters correlate with the punctual events marked in Fig. 8A.

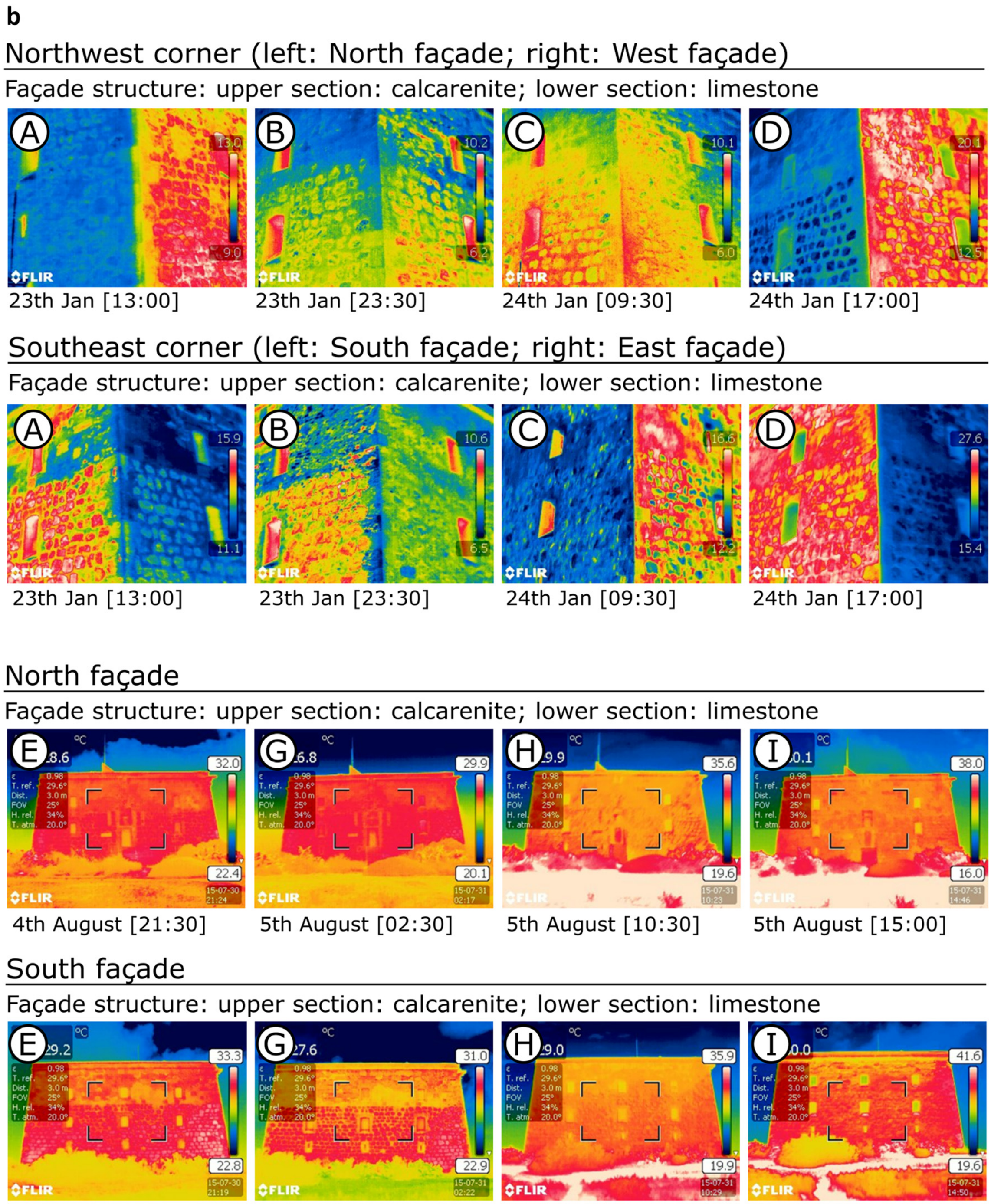

Fig. 8A (*continued*).

controlling salt crystallization (Pel et al., 2018). Due to the strong thermal change caused by solar radiation causes at surface level, related weathering processes will be especially significant in the outer few millimetres of the rock. According to the scheme in Fig. 6, calcarenite blocks in the southern façade are the most vulnerable to thermal decay, following by those in the eastern and western ones. Similar results were found by Mottershead et al. (2003), and they conclude that the maximum surface temperature reached by stone plays a significant control over rock erosion.

Wind-driven rain is widely accepted to be the most aggressive erosion agent for stone cultural heritage, especially in rainy regions (Erkal et al., 2012). Alicante region is classified as a "sheltered exposure" area due mainly to the very low rainfall, and consequently, the effects of wind-driven rain in the architectural heritage are expected to be modest (Pérez-Bella et al., 2012). However, in this classification the intensity of the rainy event is not taken into account. The Nueva Tabarca climate is characterized by torrential rains during autumn and winter. During these extreme events, rainfall intensities higher than 20 mm/h have been registered (Martínez-Martínez et al., 2017a). The maximum intensity of these heavy rainfalls is of brief duration (less than 30 min), but the rainy event can last up to 90 min with moderate-high intensity. The damages (material erosion) caused by wind-driven rain depend on the impact angle of rain drops, the wind and drop velocity and the drop size (Erkal et al., 2012). There are not any specific studies about the aggressiveness of the wind-driven rain in Mediterranean semiarid climates, but it is globally accepted that the higher the intensity, the bigger the raindrop size, and consequently, the higher the erosive power of the rainfall (Erkal et al., 2012). It is not possible to consider wind-driven rain as a dominant weathering process in Nueva Tabarca Island due to the sporadic nature of these torrential precipitations. However, their extremely high intensity and aggressiveness, in addition to their occasional occurrence, can contribute to explain unpredictable, episodic, and sometimes catastrophic stone breakdowns (Smith et al., 2010).

Finally, it is important to highlight that the maximum erosion depths were measured in the calcarenite blocks of the eastern façade, whilst minimum values were found on blocks of the northern face. Maximum wind-driven rain intensities were obtained in both east and north directions. This suggests that the effective erosive capacity of the wind-driven rain is controlled by the intensity of the weathering processes acting on the stone surface previously. The eastern façade is the only one where the intense wind-driven rain acts on a rock surface already moderately weathered by the thermal action of solar radiation. Despite heavy wind-driven rain on the northern face, rock surface is only slightly affected by previous decay processes, and consequently, the effectivity of erosive agents is low in general terms. Contrarily, solar radiation is moderately and highly aggressive in western and southern façades, respectively, but the intensity of the wind-driven rain in these directions is low. The erosive effectivity of the sporadic storms in west and south directions is high due to the pre-existing condition of the stone surface. As a result, the total erosion of the stone ashlars in these walls is moderate.

Therefore, total erosion of stone surface is the result of several processes acting simultaneously and subsequently. Firstly, different simultaneous weathering agents weaken the surface material. Secondly, erosion agents remove the decayed layers. Maximum recession depths develop on blocks where both weathering and erosion agents act intensely. In this study, solar radiation and the indirect processes arising therefrom, were found to be the most important weathering agents. Wind-driven rain is the main erosion agent, especially in Mediterranean semiarid climates due to its torrential nature (Martínez-Martínez et al., 2017a).

All these results highlight the interest of the newly proposed methodology for both surface erosion quantification and anisotropy analysis of the weathering system. However, conclusions were drawn from observations over a two-year period. Further work, using the same methodology but including longer climatic series, is needed to corroborate and to extrapolate the obtained results. Future research lines will also focus on two relevant points: 1) analyzing the aspect-related variability of the weathering pattern developed in the calcarenite ashlars; and 2) comparing the anisotropy matrix obtained in the semiarid Mediterranean climate with other different climates.

6.2. Hazard, modulated hazard and vulnerability of calcarenites and limestones

The parameters 'hazard', 'vulnerability' and 'exposure' are considered independent variables in the probabilistic assessment of the 'loss of surface material' carried out by Erkal et al. (2012) (Eq. (1)). However, our results reveal that 'hazard' and 'exposure' cannot be treated independently. The aggressiveness of the weathering system ('hazard') is not a global concept, for the types of processes involved in the rock weathering and their intensity depend strongly on the orientation ('exposure') of the studied element. For example, "hazard" levels can be considered relatively high in Nueva Tabarca Island due to the fact that local climatic conditions favour sea salt crystallization, wind erosion, and thermal cracking during the extreme thermal shock caused by the intense solar radiation that characterizes the semiarid Mediterranean climate. However, the monitored conditions on the studied northern face of the San José Tower, for instance, create generate moderate-low weathering intensity and, consequently, a moderate-low hazard, whilst these parameters are high or very high in the east and south directions.

A unique variable, named "modulated hazard", is proposed to be used instead of "hazard" and "exposure". "Modulated hazard" includes both (1) the specific weathering agents that act on specific exposures; and (2) the proportional intensity with which each decay process affects the rock. In the current case study, high modulated hazard is obtained for eastern exposures, moderate values for southern and western orientations, and finally, low modulated hazard was determined on the northern faces. As a consequence, the appropriate "modulated hazard" could be used to assess the real risk of loss of an element knowing its specific aspect. Future works will be focused on the quantification of this new parameter in terms of both intensity and frequency of occurrence of different weathering events. This new parameter will be expressed in the vector space in order to include the concept of directionality.

'Vulnerability' in Eq. (1) is understood as rock susceptibility. This parameter introduces the idea that rock erosion depends not only on the aggressiveness of the surrounding environment, but also on the intrinsic properties of stone and its resistance to weathering processes. The higher the vulnerability, the higher the susceptibility to be weathered and eroded. This parameter, unlike 'hazard' and 'exposure', is independent from the anisotropy of the weathering system.

Rock vulnerability is determined by several petrographic and petrophysical factors, including: (1) porosity; (2) mean pore size and pore size distribution; (3) the facility of water/solution transport through the porous system, in terms of solution supply rate during salt crystallization processes, water supply for freeze-thaw mechanisms, or water evaporation; and (4) strength, which is the material's resistance to the stresses generated during the weathering and erosion processes (Benavente et al., 2004; Benavente et al., 2007; Ruedrich and Siegesmund, 2007; Di Benedetto et al., 2015).

Building materials used in the San José Tower offer an example of how the intrinsic vulnerability of two different rocks determine their final erosion degree. Properties showed in Table 1 demonstrate that calcarenite and limestone blocks have contrasting hydro-mechanical properties. As a consequence of the higher porosity and the lower mechanical resistance of calcarenite, it is decayed much easier than the limestone during weathering processes such as salt crystallization or thermal degradation. Moreover, the low strength of calcarenite makes this building material highly vulnerable to the erosion during heavy wind-driven rain events (Vergès-Belmin, 2010).

However, it is important to note that the parameter 'vulnerability' expresses the potential ease to develop damages during decay processes, but the real deterioration is also controlled by the previously discussed 'modulated hazard', as expressed in Eq. (1). For example, although the calcarenite was found to have higher intrinsic vulnerability to weathering and erosion than the limestone, calcarenite blocks of the north face of the San José Tower show similar deterioration degrees to limestone blocks (Figs. 4 and 5) because microclimatic conditions in the north face are less damaging than in the rest of the faces. This is a clear example of the complex relationship between rock susceptibility, aspect and environmental aggressiveness.

7. Conclusions

A new methodology was proposed to quantify both the intensity and the anisotropy of weathering agents, including directionality and seasonality. The newly proposed *anisotropy matrix* integrates all this information. It is defined through three *anisotropic vectors* that represent the anisotropic degree of the three studied directional variables (wind, wind-driven rain, and solar radiation). In the analysed case study, the most anisotropic variables during the studied period were wind-driven rain ($\overrightarrow{A}^{n}_{wdr}$ =(2.07,0.53)) and solar radiation ($\overrightarrow{A}^{n}_{sr}$ =(-1.64,0.69)). Wind also shows a slight directionality in spring (north) and summer (south), but this seasonal anisotropy is compensated on the annual scale, and displays a quasi-isotropic behaviour.

Precise recession depths were measured on the San José Tower of Nueva Tabarca Island by analyzing point clouds obtained from a 3D photogrammetric model captured using a multi-rotor unmanned aerial vehicle (UAV). The maximum erosion depths were encountered on the calcarenite blocks of the eastern façade (maximum recession depth of 26.77 mm), whilst minimum values were obtained on blocks of the northern face (6.37 mm). Wind-driven rain is widely accepted to be the most aggressive erosion agent of stone cultural heritage. However, maximum wind-driven rain intensities were obtained in both east (where maximum erosion was measured) and north directions (minimum erosion), which challenges pre-established theories. It suggests that the effective erosive capacity of the wind-driven rain is controlled by the intensity of weathering processes that acted previously on the stone surface. In the analysed case study, rapid surface temperature increments (up to 17.5 °C) were observed and attributed to solar radiation, and this was proposed to be one of the most significant weathering agents.

According to our results, weathering agents act as conditioning factors of the subsequent erosion process; the most eroded façades of the studied monument are not those exposed to intense erosion agents (rain, wind and wind-driven rain), but those where weathering and erosion agents act simultaneously with moderate-high intensity. This conclusion confirms globally accepted theories about the consecutive relationship between weathering and erosion, suggesting that without previous weathering, the erosion does not happen. Obtained results support this theory and the idea that non-weathered surfaces can show low-level damages despite severe erosive episodes. In light of the above, the thorough understanding and accurate quantification of the anisotropic character of the weathering system becomes even more important in order to control and carry out preventive actions against surface deterioration of monuments. In this sense, results obtained in this paper contribute to the United Nations' 2030 Agenda for Sustainable Development.

The obtained results demonstrate that 'hazard' (or aggressiveness) and 'exposure' cannot be treated independently, as in previous works. These parameters are co-dependent due to the directionality and intrinsic anisotropy of the rock weathering system. "Modulated hazard" is proposed as a unique variable, including both (1) the specific weathering agents that act under specific exposures; and (2) the proportional intensity at which each decay process affects the rock. Contrarily, the term "vulnerability" defines the observed behaviour of the two different types of building materials in the San José Tower (a massive limestone and a porous calcarenite). They provide an excellent example of how the intrinsic vulnerability of two rocks determine their final erosion degree.

CRediT authorship contribution statement

J. Martínez-Martínez: Conceptualization, Methodology, Writing – original draft, Visualization. **A. Abellán:** Investigation, Formal analysis, Methodology, Writing – review & editing. **E. Berrezueta:** Visualization, Writing – review & editing.

Declaration of competing interest

The authors declare that they have no known competing financial interests or personal relationships that could have appeared to influence the work reported in this paper.

Acknowledgments

This research was supported by the Spanish Government (MICINN) (PID2020-116896RB-C21 and PID2020-116896RB-C22).

References

Agisoft, 2017. Agisoft PhotoScan User Manual: Professional Edition, Version 1.3. http://www.agisoft.com/pdf/photoscan-pro_1_3_en.pdf.

Almqvist, B.S., Mainprice, D., 2017. Seismic properties and anisotropy of the continental crust: predictions based on mineral texture and rock microstructure. Rev. Geophys. 55 (2), 367–433.

ASTM D5731 – 95: Standard Test Method for Determination of the Point Load Strength Index of Rock. ASTM International, West Conshohocken, PA.

Benavente, D., García-del-Cura, M.A., Fort, R., Ordóñez, S., 2004. Durability estimation of porous building stones from pore structure and strength. Eng. Geol. 74, 113–127.

Benavente, D., Martínez-Martínez, J., Cueto, N., García-del-Cura, M.A., 2007. Salt weathering in dual-porosity building dolostones. Eng. Geol. 94, 215–226.

Benavente, D., Cultrone, G., Gómez-Heras, M., 2008. The combined influence of mineralogical, hygric and termal properties on the durability of porous building stones. Eur. J. Mineral. 20, 673–685. https://doi.org/10.1127/0935-1221/2008/0020-1850.

Blocken, B., Carmeliet, J., 2006. On the validity of the cosine projection in wind-driven rain calculations on buildings. Build. Environ. 41 (9), 1182–1189.

Blocken, B., Carmeliet, J., 2010. Overview of three state-of-the-art wind-driven rain assessment models and comparison base on model theory. Build. Environ. 45 (3), 691–703.

Brimblecombe, P., Grossi, C.M., Harris, I., 2011. Climate change critical to cultural heritage. In: Gökçekus, H., Türker, U., LaMoreaux, J.V. (Eds.), Survival and Sustainability, Environmental Concerns in the 21st Century. Springer, Berlin Heidelberg, pp. 91–101.

Clarke, A.P., Vannucchi, P., 2020. Structural anisotropy: using image analysis to quantify block-in-matrix fabrics. J. Struct. Geol. 131, 103939.

Corbí, H., Martínez-Martínez, J., Martín-Rojas, I., 2019. Linking geological and architectural heritage in a singular geosite: Nueva Tabarca island (SE Spain). Geoheritage 11, 703–716.

Demoulin, T., Girardet, F., Wangler, T.P., Scherer, G.W., Robert, J.F., 2016. On-site monitoring for better selection of stone repairs: a case study. Herit. Sci. 4, 38. https://doi.org/10.1186/s40494-016-0108-z.

Di Benedetto, C., Cappelletti, P., Favaro, M., Graziano, S.F., Langella, A., Calcaterra, D., Colella, A., 2015. Porosity as key factor in the durability of two historical building stones: Neapolitan Yellow Tuff and Vicenza Stone. Eng. Geol. 193, 310–319.

Díez-Herrero, A., Gutiérrez-Pérez, I., Lario, J., Cañaveras, J.C., Benavente, D., Sánchez-Moral, S., Alonso-Azcárate, J., 2009. Analysis of potential direct insolation as a degradation factor of cave paintings in Villar del Humo, Cuenca, Central Spain. Geoarchaeology 24 (4), 450–465. https://doi.org/10.1002/gea.20274.

Erkal, A., D'Ayala, D., Sequeira, L., 2012. Assessment of wind-driven rain impact, related surface erosion and surface strength reduction of historic building materials. Build. Environ. 57, 336–348.

Fatoric, S., Seekamp, E., 2017. Are cultural heritage and resources threatened by climate change? A systematic literature review. Clim. Chang. 144, 227–254. https://doi.org/10.1007/s10584-017-1929-9.

Frydman, M., Pacheco, F., Pastor, J., Canesin, F.C., Caniggia, J., Davey, H., 2016. Comprehensive determination of the far-field earth stresses for rocks with anisotropy in tectonic environment. SPE Argentina Exploration and Production of Unconventional Resources Symposium. OnePetro.

Fu, P., Rich, P.M., 1999. Design and implementation of the solar analyst: an ArcView extension for modelling solar radiation at landscape scales. Proceedings of the 19th Annual ESRI User Conference.

Gizzi, F.T., Sileo, M., Biscione, M., Danese, M., Alvarez de Buergo, M., 2016. The conservation state of the Sassi of Matera site (Southern Italy) and its correlation with the environmental conditions analysed through spatial analysis techniques. J. Cult. Herit. 17, 61–74. https://doi.org/10.1016/j.culher.2015.05.002.

Grossi, C.M., Brimblecombe, P., Menéndez, B., Benavente, D., Harris, I., Déqué, M., 2011. Climatology of salt transitions and implications for stone weathering. Sci. Total Environ. 409, 2577–2585. https://doi.org/10.1016/j.scitotenv.2011.03.029.

Hall, K., Thorn, C., Sumner, P., 2012. On the persistence of 'weathering'. Geomorphology 149–150, 1–10. https://doi.org/10.1016/j.geomorph.2011.12.024.

ICOMOS-ISCS, 2008. Illustrated glossary on stone deterioration patterns. http://international.icomos.org/publications/monuments_and_sites/15/pdf/Monuments_and_Sites_15_ISCS_Glossary_Stone.pdf.

Lacy, R.E., Shellard, H.C., 1962. An index of driving rain. Meteorol. Mag. 91 (1080), 177e84.

Laque, D., Brodu, N., Leroux, J., 2013. Comparison of complex topography with terrestrial lased scanner: application to the Rangitikei canyon (N-Z). ISPRS J. Photogramm. Remote Sens. 82, 10–26. https://doi.org/10.1016/j.isprsjprs.2013.04.009.

Martínez-Martínez, J., Benavente, D., Jiménez Guitérrez, S., García-del-Cura, M.A., Ordóñez, S., 2017a. Stone weathering under Mediterranean semiarid climate in the fortress of Nueva tabarca island (Spain). Build. Environ. 121, 262–276. https://doi.org/10.1016/j.buildenv.2017.05.034.

Martínez-Martínez, J., Corbí, H., Martin-Rojas, I., Baeza-Carratalá, J.F., Giannetti, A., 2017b. Stratigraphy, petrophysical characterization and 3D geological modelling of the historical quarry of Nueva Tabarca island (western Mediterranean): implications on the heritage conservation. Eng. Geol. 231, 88–99. https://doi.org/10.1016/j.enggeo.2017.10.014.

McAllister, D., Warke, P., McCabe, S., 2017. Stone temperature and moisture variability under temperate environmental conditions: implications for sandstone weathering. Geomorphology 280, 137–152. https://doi.org/10.1016/j.geomorph.2016.12.010.

Micheletti, N., Chandler, J.H., Lane, S.N., 2015. Structure from motion (SFM) photogrammetry. In: Clarke, L.E., Nield, J.M. (Eds.), Geomorphological Techniques, Online edition 2047-0371. British Society for Geomorphology, London.

Mottershead, D., Gorbushina, A., Lucas, G., Wright, J., 2003. The influence of marine salts, aspect and microbes in the weathering of sandstone in two historic structures. Build. Environ. 38, 1193–1204.

Novitsky, C.G., Holbrook, W.S., Carr, B.J., Pasquet, S., Okaya, D., Flinchum, B.A., 2018. Mapping inherited fractures in the critical zone using seismic anisotropy from circular surveys. Geophys. Res. Lett. 45 (7), 3126–3135.
Pel, L., Pishkari, R., Casti, M., 2018. A simplified model for the combined wicking and evaporation of a NaCl solution in limestone. Mater. Struct. 55, 66–76. https://doi.org/10.1617/s11527-018-1187-y.
Pérez-Bella, J.M., Domínguez-Hernández, J., Rodríguez-Soria, B., del Coz-Díaz, J.J., Cano-Suñén, E., 2012. Estimation of the exposure of buildings to driving rain in Spain from daily wind and rain data. Build. Environ. 57, 259–270.
Ruedrich, J., Siegesmund, S., 2007. Salt and ice crystallization in porous sandstones. Environ. Geol. 52, 369–381.
Ruedrich, J., Kirchner, D., Siegesmund, S., 2011. Physical weathering of building stones induce by freeze-thaw action: a laboratory long-term study. Environ. Earth Sci. 63, 1573–1586. https://doi.org/10.1007/s12665-010-0826-6.
Sancho, C., Fort, R., Belmonte, A., 2003. Weathering rates of historic sandstone structures in semiarid environments (Ebro basin, NE Spain). Catena 53, 53–64. https://doi.org/10.1016/S0341-8162(02)00197-2.
Shi, X.J., Shi, X.F., 2014. Numerical prediction on erosion damage caused by wind-blown sand movement. Eur. J. Environ. Civ. En. 18, 550–566.
Smith, B.J., Gomez-Heras, M., Viles, H.A., 2010. Underlying Issues on the Selection, Use and Conservation of Building Limestone. 331. Geological Society Special Publication, London, pp. 1–11.
Stumpf, A., Malet, J.-P., Kerle, N., Niethammer, U., Rothmund, S., 2013. Image-based mapping of surface fissures for the investigation of landslide dynamics. Geomorphology 186, 12e27. https://doi.org/10.1016/j.geomorph.2012.12.010.
UNE-EN 12370, 1999. Métodos de ensayo para piedra natural. Determinación de la resistencia a la cristalización de sales. AENOR–CEN.
UNE-EN 14157, 2005. Natural Stone Test Methods. Determination of the Abrasion Resistance. AENOR–CEN.
Vergès-Belmin, V., 2010. Deterioration of stone in monuments. In: Schrefler, B., Delage, P. (Eds.), Environmental Geomechanics. ISTE Ltd, London (UK).
Waragai, T., Hiki, Y., 2019. Influence of microclimate on the directional dependence of sandstone pillar weathering in Angkor Wat temple, Cambodia. Prog. Earth Planet. Sci. 6, 10. https://doi.org/10.1186/s40645-019-0254-5.
Wu, Y., Li, Y., Luo, S., Lu, M., Zhou, N., Wang, D., Zhang, G., 2020. Multiscale elastic anisotropy of a shale characterized by cross-scale big data nanoindentation. Int. J. Rock Mech. Min. Sci. 134, 104458.
Zhao, D., Lu, W., Wang, Y., Mao, X., Ai, Y., Jiang, H., 2016. Experimental studies on earthen architecture sites consolidated with BS materials in arid regions. Adv. Mater. Sci. Eng. 2016 (2), 1–13.